Cryo-EM structure of the DNA-PK holoenzyme

Humayun Sharif[a,b,1], Yang Li[a,b,1], Yuanchen Dong[c], Liyi Dong[a,b], Wei Li Wang[c], Youdong Mao[c,d,e], and Hao Wu[a,b,2]

[a]Department of Biological Chemistry and Molecular Pharmacology, Harvard Medical School, Boston, MA 02115; [b]Program in Cellular and Molecular Medicine, Boston Children's Hospital, Boston, MA 02115; [c]Department of Cancer Immunology and Virology, Intel Parallel Computing Center for Structural Biology, Dana-Farber Cancer Institute, Boston, MA 02215; [d]Department of Microbiology and Immunobiology, Harvard Medical School, Boston, MA 02115; and [e]State Key Laboratory for Artificial Microstructures and Mesoscopic Physics, School of Physics, Center for Quantitative Biology, Peking University, Beijing 100871, China

Contributed by Hao Wu, June 2, 2017 (sent for review May 4, 2017; reviewed by Michael R. Lieber and Michael G. Rossmann)

DNA-dependent protein kinase (DNA-PK) is a large protein complex central to the nonhomologous end joining (NHEJ) DNA-repair pathway. It comprises the DNA-PK catalytic subunit (DNA-PKcs) and the heterodimer of DNA-binding proteins Ku70 and Ku80. Here, we report the cryo-electron microscopy (cryo-EM) structures of human DNA-PKcs at 4.4-Å resolution and the DNA-PK holoenzyme at 5.8-Å resolution. The DNA-PKcs structure contains three distinct segments: the N-terminal region with an arm and a bridge, the circular cradle, and the head that includes the kinase domain. Two perpendicular apertures exist in the structure, which are sufficiently large for the passage of dsDNA. The DNA-PK holoenzyme cryo-EM map reveals density for the C-terminal globular domain of Ku80 that interacts with the arm of DNA-PKcs. The Ku80-binding site is adjacent to the previously identified density for the DNA-binding region of the Ku70/Ku80 complex, suggesting concerted DNA interaction by DNA-PKcs and the Ku complex.

DNA repair | V(D)J recombination | NHEJ | cryo-EM | structure

DNA double-strand breaks (DSBs) are essential for certain physiological processes but pose threats to genetic integrity and cell viability in pathological conditions (1). Programmed physiological DSBs can be generated in lymphoid cells during genetic rearrangements by the recombination-activating gene (RAG) enzyme complex in variable (V), diversity (D), and joining (J) gene segments [V(D)J] recombination and during antibody response by activation-induced cytidine deaminase (AID) in class-switch recombination (2, 3). In contrast, pathological DSBs are generated in cells by various insults, including reactive oxygen species, ionizing radiations, RAG and AID off-target effects, and topoisomerase I failures. Eukaryotic cells have evolved two discrete and complementary DSB repair pathways: homologous recombination and nonhomologous end joining (NHEJ) (1, 2). Although homologous recombination is predominantly used during the S and G2 phases of the cell cycle for error-free repair of pathological DSBs, NHEJ is favored in all stages of a cell cycle, does not need any homology, and is used for repair of both physiological and pathological DSBs (2).

NHEJ requires a protein complex consisting of the heterodimer of Ku70 and Ku80 (Ku complex) that recognizes DSB free ends (4) and the DNA-dependent protein kinase catalytic subunit (DNA-PKcs) (1, 5, 6) that recruits core NHEJ factors including Artemis, XRCC4, Ligase IV, and XLF on DSB break sites (2). DNA-PKcs is a ∼470-kDa serine-threonine kinase belonging to the phosphoinositide 3-kinase-related kinase family, which also includes mechanistic target of rapamycin (mTOR), ataxia telangiectasia mutated (ATM), ataxia telangiectasia and Rad3 related (ATR), nonsense mediated mRNA decay associated PI3K related kinase (SMG1), transformation/transcription domain-associated protein (TRRAP) (5, 7). The Ku80 C-terminal region (CTR) has been implicated in interacting with DNA-PKcs to form the DNA-PK holoenzyme (8, 9). A recent crystal structure of DNA-PKcs at 4.3-Å resolution gave improved insights into the DNA-PKcs domain architecture (10). However, despite the inclusion of a 194-residue fragment of Ku80 CTR, only two small pieces of Ku80 density were visible. Here, we present a cryo-EM structure of the DNA-PK holoenzyme that sheds light on DNA-PKcs/Ku interactions, conformational changes, and concerted DNA recognition.

Results

Cryo-EM Reconstruction of DNA-PK. We modified existing protocols (6, 11, 12) for purifying DNA-PKcs from HeLa cell nuclear extracts and found that we obtained a fraction of DNA-PKcs with an apparent stoichiometric amount of bound Ku complex, representing the DNA-PK holoenzyme (Fig. S1*A*) (6, 11, 12). We imaged the purified DNA-PK with an FEI Tecnai Arctica microscope equipped with a Gatan K2 Summit direct detector camera. Raw micrographs and 2D class averages showed mostly dispersed monomers (Fig. S1*B*). Initially, ∼1 million particles of DNA-PK were extracted. Reference-free 2D classification was performed, and ∼860K particles remained after throwing out bad classes. 3D classification showed only minor differences between the 3D classes, and we combined all particles for 3D refinement. Because orientation preference was detected, we filtered out approximately two-thirds of the particles at the preferred orientation (Fig. S1*C*). 3D refinement using the resulting ∼290K particles gave a 4.4-Å resolution map by gold standard Fourier shell correlation (FSC) (Fig. 1 *A*–*C* and Fig. S1*D*). Overall, the cryo-EM map showed defined secondary structural elements and large side chains (Fig. 1*B* and Fig. S2), and we built an atomic model of DNA-PKcs, using the recently published crystal structure (5LUQ) as the reference (10) (Fig. 1*D*, Fig. S3*A*, and Table S1). However, the cryo-EM map did not reveal the location of the Ku complex.

Structure of DNA-PKcs. The cryo-EM structure is mostly similar to the crystal structure (10) with the exception of local conformational differences, the order and disorder of several loops, and the lack of density for a 64-residue-long region in the crystal structure built with

Significance

Double-stranded DNA breaks pose a serious threat to the survival of cells. Nonhomologous end joining (NHEJ) is a crucial DNA repair pathway in which the DNA-dependent protein kinase (DNA-PK) complex, a key holoenzyme consisting of the Ku70/80 heterodimer and the catalytic subunit DNA-PKcs, senses DNA breaks and initiates the NHEJ repair pathway. Here, we present cryo-EM structures of the DNA-PK complex. Together with previous structural and biochemical studies, our structures lead to a partial model for the interactions between DNA-PKcs and the Ku70/80 complex, and reveal how the DNA-PK complex may bring free ends of damaged DNA for repair.

Author contributions: H.S. and H.W. designed research; H.S. and Y.L. performed research; H.S., Y.L., Y.D., and W.L.W. collected data; H.S., Y.L., Y.D., L.D., and Y.M. analyzed data; and H.S., Y.L., and H.W. wrote the paper.

Reviewers: M.R.L., University of Southern California; and M.G.R., Purdue University.

The authors declare no conflict of interest.

Data deposition: The atomic coordinates and cryo-EM reconstructions have been deposited in the Protein Data Bank, www.pdb.org (PDB ID 5W1R), and EMDataBank, www.emdatabank.org (ID EMD-8751 and EMD-8752).

[1]H.S. and Y.L. contributed equally to this work.

[2]To whom correspondence should be addressed. Email: wu@crystal.harvard.edu.

This article contains supporting information online at www.pnas.org/lookup/suppl/doi:10.1073/pnas.1707386114/-/DCSupplemental.

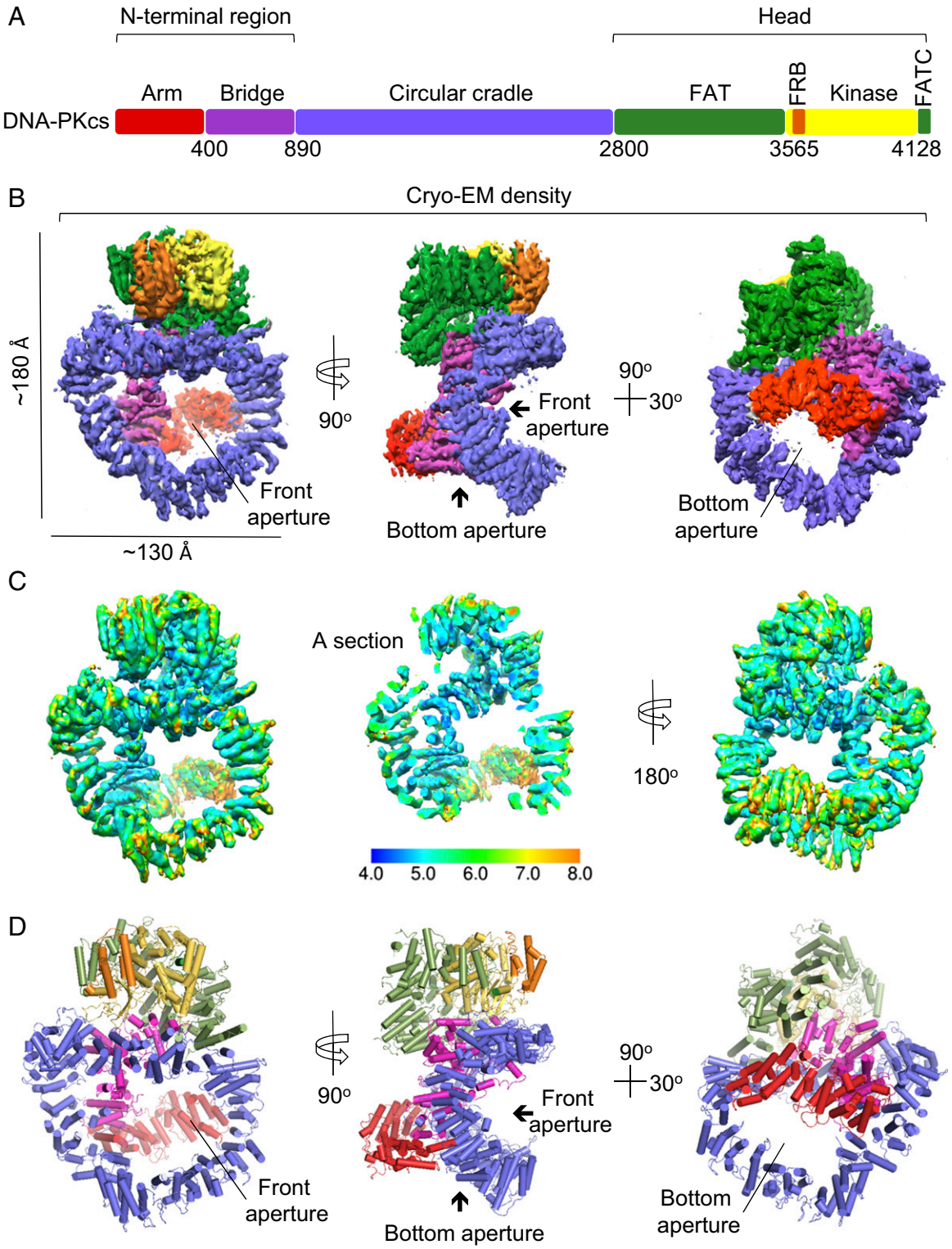

Fig. 1. The overall DNA-PKcs structure. (*A*) Schematics of DNA-PKcs domain architecture showing the three units of the DNA-PKcs structure: N-terminal region with arm (red) and bridge (magenta), the circular cradle (blue) and the head domain containing FAT (FRAP-ATM-TRRAP) (green), FRB (FKBP12-rapamycin-binding) (orange), kinase (yellow), and FATC (FAT C-terminal) (dark green) domains. (*B*) Cryo-EM density of DNA-PKcs at 4.4-Å resolution. (*C*) Overall resolution distribution of DNA-PKcs cryo-EM map. Two different views are shown on the *Left* and *Right*. (*Middle*) Cut-through section of DNA-PKcs. The resolution range is color-coded. (*D*) Cartoon representation of DNA-PKcs model in orientations similar to in *B*.

polyalanine, but assigned to be between residues 2577 and 2773 (Fig. S3*B*). Following the crystal structure nomenclature, DNA-PKcs consists of an N-terminal region, a circular cradle unit, and a head unit with the kinase domain sandwiched between FAT and FATC domains (Fig. 1). Both the N-terminal L-shaped region and the cradle unit contain HEAT repeats, and the former can be

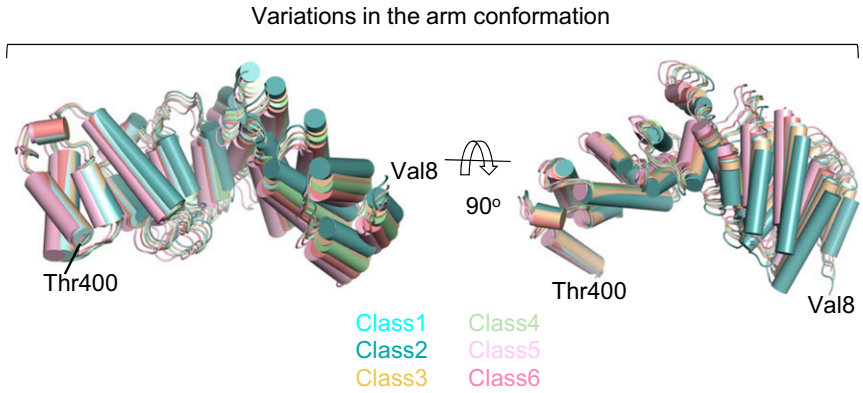

Fig. 2. Conformational dynamics of the DNA-PKcs arm. Variations in the arm conformation in six classes of cryo-EM data are shown as cartoons: class 1 (cyan), class 2 (teal), class 3 (wheat), class 4 (light green), class 5 (light magenta), and class 6 (pink).

further divided into the arm (~residues 1–400) and the bridge (~residues 401–890) (Fig. 1 *A* and *D*). The bridge connects to the top of the circular cradle and contacts the C-terminal head unit. There are two large, perpendicular apertures in the structure. In the orientation shown, the front aperture is formed by the circular cradle and the bottom aperture is formed by the arm and the bottom part of the circular cradle (Fig. 1 *B*–*D*). Local resolution estimation revealed that the arm is the most flexible (Fig. 1*C*). Three-dimensional classification into six classes starting from the final refined particle orientations, but with local search, revealed significant conformational differences in the arm among the classes (Fig. 2).

Ku80 CTR Mediates Interaction of Ku70/Ku80 with DNA-PKcs. Lack of density for the Ku complex in the cryo-EM map suggested potential heterogeneity of the DNA-PK sample. Further 3D classification revealed that three classes out of six, which include ~50% of the total particles, showed extra density near the N-terminal arm region of DNA-PKcs (Fig. S4*A*). Because only seven residues are missing at the N terminus of the DNA-PKcs model, this extra density most likely belongs to the Ku80 CTR (Fig. 3*A*), which has been shown to bind to DNA-PKcs (13, 14). One class containing 16% of the particles (~46K) had the most distinct extra density, and 3D refinement of this single class resulted in a 5.8-Å map of the DNA-PK complex with ~9-Å resolution for the Ku80 density based on local resolution estimation (Fig. 3*B* and Fig. S4*B*). That only a fraction of the DNA-PK images contained the Ku complex may be indicative of the previously assessed weak affinity of DNA-PKcs with Ku80 in the absence of DNA (15).

Previous studies have shown that the CTR of Ku80 (~residues 543–732) contains a globular domain (~residues 592–709) followed by a helix at the extreme end (13, 14) (Fig. 3*A*). In the DNA-PKcs structure cocrystallized with the CTR, only two short fragments that likely correspond respectively to the C-terminal helix of Ku80 and the linker between the globular domain and the C-terminal helix were visibly bound to DNA-PKcs (10) (Fig. 3*C*). In our cryo-EM map, neither of these segments was apparent. In contrast, the Ku80 extra density exhibits a shape that fits with the NMR structures of the Ku80 CTR globular domain (1Q2Z and 1RW2) (13, 14) (Fig. S4*C*). In the 3D class with the most prominent Ku80 density, the arm is positioned further upward in comparison with classes that do not possess this density (Fig. 3*D*). It is likely that the bound CTR globular domain pushes the arm upward on the interaction. The modeled CTR globular domain is adjacent to the presumed linker fragment of Ku80 in the crystal structure (10), further supporting that the extra density belongs to Ku80 CTR (Fig. 3*C*).

Toward a DNA-PK Holoenzyme Functional Model. To build a plausible model for the DNA-PK holoenzyme containing the DNA-binding Ku core complex, we used an ~25-Å cryo-EM map of the DNA-PK holoenzyme assembled on a DNA molecule (15). In this map, the Ku core complex density is in proximity to the Ku80 CTR that we localized in this study. However, the density does not have enough details to allow for accurate fitting of the crystal structure of the Ku complex (16). Hence, we simply placed the crystal structure by minimizing the distance between the Ku80 core and the Ku80 CTR, resulting in an imprecise, pseudoatomic model of full-length DNA-PK (Fig. 4*A*). In another cryo-EM structure of the DNA-PK/DNA complex at 21.4-Å resolution (17), the Ku density distributes in a fan shape around the extra density we identified here for the Ku80 CTR (Fig. 4*A*), showing the flexible tether to the N-terminal DNA-binding domain of the Ku complex. Intriguingly, even though the CTR used in the crystallization of DNA-PKcs includes the globular domain (10), no density was observed in the crystal structure. In the crystal lattice, the arm of one molecule contacts the head unit of a neighboring molecule (10). We speculate that the apparent CTR globular domain-induced conformational change at the arm region may be incompatible with crystal packing. In contrast, we do not know why our cryo-EM density does not show the two short Ku80 fragments observed in the crystal structure. It is possible that Ku80 interaction with DNA-PKcs is much more complex and that one scenario evokes multiprong interactions between Ku80 and DNA-PKcs.

Discussion

Our DNA-PK structure provides a foundation to elucidate how DNA-PKcs and the Ku70/80 complex interact with and repair the DNA broken ends. Both the front and the bottom apertures in DNA-PKcs are large enough to allow the passage of dsDNA. Because the bottom aperture contains the putative DNA-binding site at the arm region (10, 17–19), and the EM map of the DNA-PK dimer at 33-Å resolution (15) positions the two bottom apertures close to each other, we modeled a dsDNA with the free end entering at the bottom aperture and the distal end exiting from the front aperture (Fig. 4B and Fig. S5*A*). Although this putative DNA location is highly speculative, it is notable that the free ends of the modeled DNA strands approach each other in this configuration (Fig. S5*B*), which may facilitate repair. It has been proposed that Ku first binds to damaged, free DNA ends, and the recruitment of DNA-PKcs induces inward translocation of Ku (20). Ku80 CTR is connected to core Ku70/80 DNA-binding domains via a long flexible linker (21), making it possible to grab either the free end, as proposed for the initial DNA interaction, or translocate to the distal end when it hands the free end to DNA-PKcs.

In summary, our cryo-EM structure of DNA-PK revealed a binding site for the Ku80 globular domain at the arm region of DNA-PKcs, which is adjacent to the general location of the

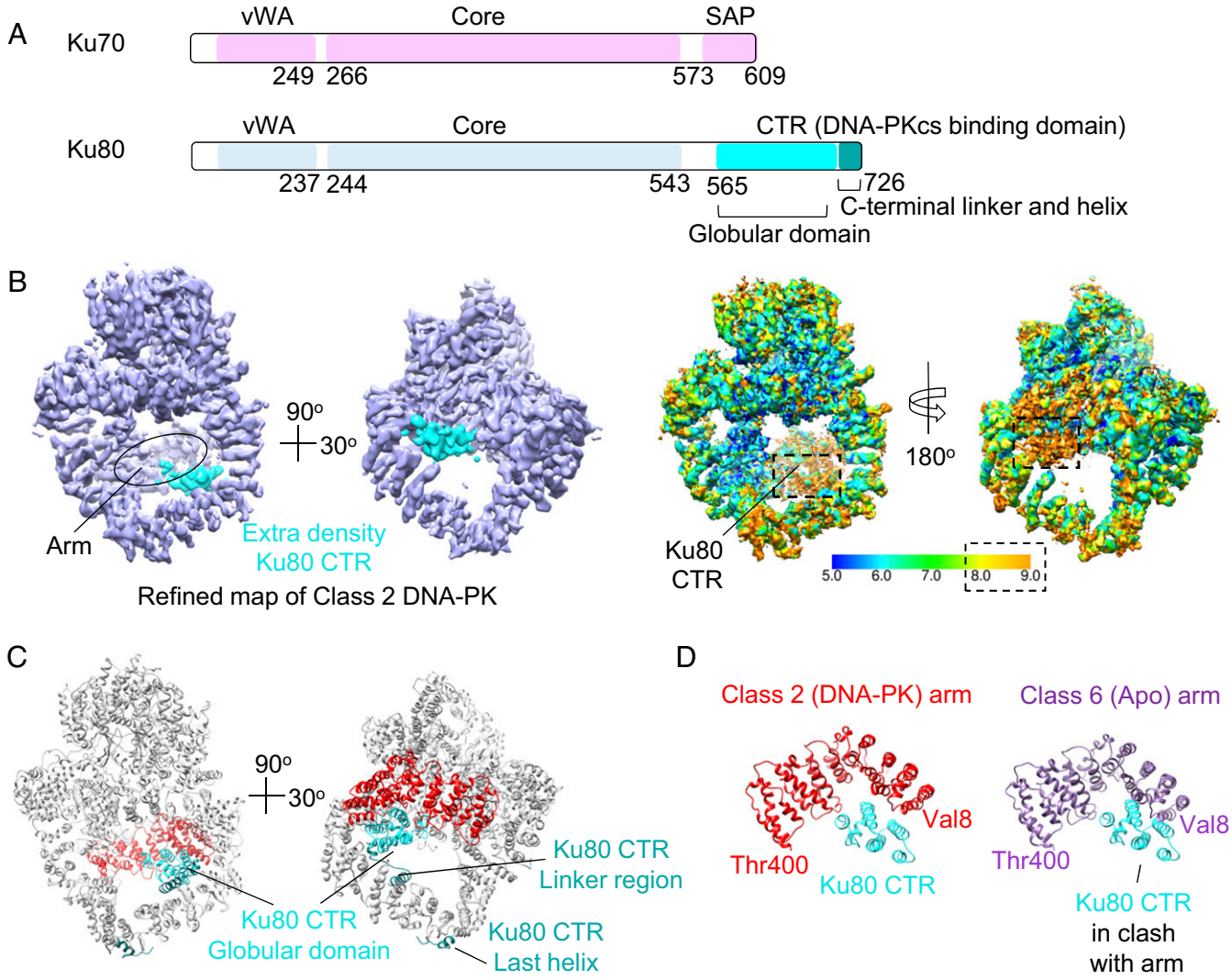

Fig. 3. DNA-PK cryo-EM structure reveals Ku80 CTR binding site. (*A*) Schematics of Ku70 and Ku80 domains. (*B*) Cryo-EM density of refined DNA-PK in class 2 at 5.8-Å resolution. (*Left*) Two panels showing the proposed Ku80 CTR density (cyan). (*Right*) Two panels showing the resolution distribution of DNA-PK with color-coded resolution range. (*C*) DNA-PK structure with highlighted structural features: arm (red), Ku80 CTR globular domain (cyan), and modeled Ku80 CTR linker and last helix fragments from the crystal structure [Protein Data Bank (PDB): 5LUQ] (teal). (*D*) Ku80 CTR globular domain (cyan) may have moved the arm (red) upward in the class 2 map. If the Ku80 CTR globular domain exists in the class 6 map, it would have been in clash with the arm (purple).

Ku70/Ku80 DNA-binding domains. The long flexible linker between the Ku80 CTR and the core Ku70/80 DNA-binding domains may allow concerted DNA binding and Ku translocation. The conformational dynamics of the arm and its apparent movement on Ku80 interaction suggest Ku and the bound DNA may allosterically activate DNA-PK through conformational remodeling, which may further help recruit other NHEJ factors for repair of damaged DNAs.

Materials and Methods

Protein Purification. HeLa S3 cell (Sigma-Aldrich) nuclear extracts were prepared as described (11). DNA-PKcs and DNA-PK complex were purified from HeLa cell nuclear extract with a protocol slightly modified from that described previously, using five sequential columns, Sepharose Hitrap Q, heparin, Mono S, Mono Q, and Superose 6 (6, 12, 15). The modification includes a step gradient elution from the heparin column instead of a linear gradient. All proteins (DNA-PKcs, Ku70, and Ku80) were confirmed by fingerprinting mass spectrometry.

EM Data Acquisition. For preparation of negative-stain grids, purified DNA-PK sample (3 μL) was applied to glow-discharged grids (Carbon Type-B, 200 mesh; Ted Pella), washed with water once, prestained with 1% (wt/vol) uranyl formate for 10 s, and then stained again for 40 s. Negative stained DNA-PK data were collected using a FEI Tecnai F20 transmission electron microscope operated at 120 kV and a 4K × 4K Gatan CCD camera. The nominal magnification was 50,000×, and the pixel size was 2.18 Å. In total, 434 images were collected.

For preparation of cryo-EM grids, purified DNA-PK sample (3 μL) was applied to glow discharged C-flat holey carbon grids (1.2/1.3, 400 mesh). The grids were plunged into liquid ethane using Vitrobot Mark IV at 4 °C and 100% humidity. Cryo-EM data were collected on a FEI Tecnai Arctica microscope operated at 200 kV, equipped with a Gatan K2 Summit direct detector detector. Specifically, movie mode image stacks were collected semiautomatically with the Leginon software (22) under superresolution counting mode, at a nominal magnification of 23,500×, which corresponds to a physical pixel size of 1.51 Å and a superresolution pixel size of 0.76 Å. Each movie stack contains 36 frames with a total exposure time of 9 s and an accumulated dose ~40 e/Å^2. A total of 5,715 image stacks were collected.

Image Processing. SAMUEL (Simplified Application Managing Utilities for EM Labs) scripts and Relion (23) were used to process both negative-stained and cryo-EM images. CTFFIND3 (24) was used to determine defocus for all datasets. For negative-stain data processing, all images were first 2 × 2 binned to a pixel

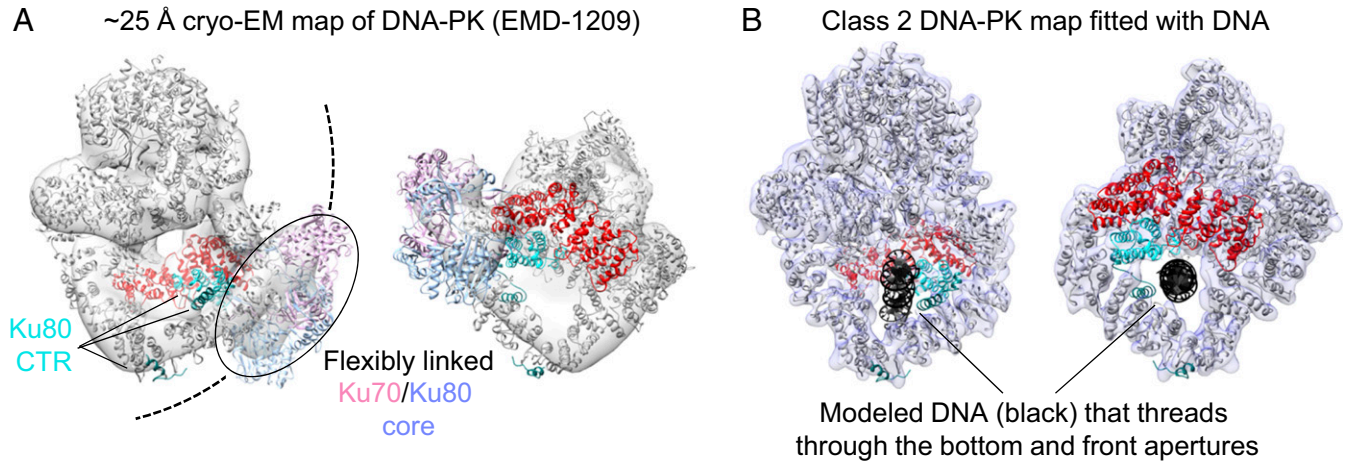

Fig. 4. A structural model for the DNA-PK interaction with DNA. (*A*) Two views of a previously reported DNA-PK map at 25-Å resolution (EMD-1209, gray), fitted with our DNA-PK structure (gray) that contains DNA-PKcs and Ku80 CTR, and with the Ku70/80 core crystal structure (PDB: 1JEY, pink and slate). The fitted orientation of the Ku70/80 core is only approximate and was achieved by placing the Ku80 core close to the Ku80 CTR. The circle highlights the Ku70/80 core domains that mediate DNA binding. The proposed movement of the core domains resulting from the flexible linker between the Ku80 core and the CTR is shown as dashed black curvy lines. (*B*) 30-bp DNA duplex (black) modeled in the DNA-PK structure. (*Left*) DNA distal end at the front aperture. (*Right*) DNA free end at the bottom aperture.

size of 4.36 Å. Initially, 19,953 particles were extracted, and Relion was used for subsequent 2D classification, 3D classification, and refinement.

For cryo-EM data, superresolution image stacks were first subjected to motion correction (25) and binned 2×2 times, resulting in a pixel size of 1.51 Å. The defocus range for DNA-PK data was from 0.5 to 3.4 μm. At first, ~3,000 particles were manually picked from a subset of images and input for 2D classification in SAMUEL. Six best 2D averages were selected as templates for autopicking with SAMUEL. After manual inspection and screening, 1,086,055 particles were selected and extracted. After 2D classification with ROME2D (26), bad classes were discarded and 855,916 particles remained. An initial model was first generated from the cryo-EM data, using the refined map from the negative stained data. This model was then used as a reference for 3D classification into six classes in Relion. Because all six classes from 3D classification were of similar overall quality and showed no significant conformational variations, we combined all particles for a few rounds of global refinement in Relion. To reduce the data size, we discarded about two thirds of the entire particles from those in preferred orientations based on _rlnMaxValueProbDistribution index. We also re-extracted the remaining 289,798 particles from dose-fractionated images, which contain subframes 3–18, and performed refinement in Relion to yield a 4.4-Å map. Local resolution was estimated using ResMap (27). To analyze potential DNA-PK heterogeneity, we reclassified the data into six classes, using the final refined orientation with local refinement in Relion. Among them, three classes contained extra densities close to the N terminus, with one of them being particularly significant. The 3D refinement in Relion using particles from this single class (16%) led to a 5.8-Å map. The NMR structure of Ku80 CTR was readily fitted into the density and modified accordingly. All resolutions were measured by golden standard FSC curves with a 0.143 cutoff.

Structure Refinement and Model Building. Crystal structure 5LUQ.pdb (10) was used as an initial model and rigid body fitted into the cryo-EM map, using UCSF Chimera (28). COOT (29) was used for fragment rebuilding and manual adjustment of side chain rotamers to best fit the cryo-EM density map. On placing the density map and the model into an artificial unit cell, we used the PHENIX software suite (30) for iterative, phased refinement in reciprocal space. The quality of the final model was analyzed using Molprobity (31).

ACKNOWLEDGMENTS. We thank Shuobing Chen for help with cryo-EM data collection. The work was supported by the National Institutes of Health (AI125535 to H.W.), by an Intel academic grant to Y.M., and by a grant of the Thousand-Talent Plan of China to Y.M. The cryo-EM facility was funded through NIH Grant AI100645, Center for HIV/AIDS Vaccine Immunology and Immunogen Design (CHAVI-ID). The experiments were performed in part at the Center for Nanoscale Systems at Harvard University, a member of the National Nanotechnology Infrastructure Network, which is supported by the National Science Foundation under Award ECS-0335765.

1. Khanna KK, Jackson SP (2001) DNA double-strand breaks: Signaling, repair and the cancer connection. *Nat Genet* 27:247–254.
2. Lieber MR (2010) The mechanism of double-strand DNA break repair by the nonhomologous DNA end-joining pathway. *Annu Rev Biochem* 79:181–211.
3. Alt FW, Zhang Y, Meng FL, Guo C, Schwer B (2013) Mechanisms of programmed DNA lesions and genomic instability in the immune system. *Cell* 152:417–429.
4. Downs JA, Jackson SP (2004) A means to a DNA end: The many roles of Ku. *Nat Rev Mol Cell Biol* 5:367–378.
5. Smith GC, Jackson SP (1999) The DNA-dependent protein kinase. *Genes Dev* 13:916–934.
6. Gell D, Jackson SP (1999) Mapping of protein-protein interactions within the DNA-dependent protein kinase complex. *Nucleic Acids Res* 27:3494–3502.
7. Morris EP, et al. (2011) Evidence for a remodelling of DNA-PK upon autophosphorylation from electron microscopy studies. *Nucleic Acids Res* 39:5757–5767.
8. Singleton BK, Torres-Arzayus MI, Rottinghaus ST, Taccioli GE, Jeggo PA (1999) The C terminus of Ku80 activates the DNA-dependent protein kinase catalytic subunit. *Mol Cell Biol* 19:3267–3277.
9. Gottlieb TM, Jackson SP (1993) The DNA-dependent protein kinase: Requirement for DNA ends and association with Ku antigen. *Cell* 72:131–142.
10. Sibanda BL, Chirgadze DY, Ascher DB, Blundell TL (2017) DNA-PKcs structure suggests an allosteric mechanism modulating DNA double-strand break repair. *Science* 355:520–524.
11. Nilsen TW (2013) Preparation of nuclear extracts from HeLa cells. *Cold Spring Harb Protoc* 2013:579–583.
12. Sibanda BL, Chirgadze DY, Blundell TL (2010) Crystal structure of DNA-PKcs reveals a large open-ring cradle comprised of HEAT repeats. *Nature* 463:118–121.
13. Harris R, et al. (2004) The 3D solution structure of the C-terminal region of Ku86 (Ku86CTR). *J Mol Biol* 335:573–582.
14. Zhang Z, et al. (2004) Solution structure of the C-terminal domain of Ku80 suggests important sites for protein-protein interactions. *Structure* 12:495–502.
15. Spagnolo L, Rivera-Calzada A, Pearl LH, Llorca O (2006) Three-dimensional structure of the human DNA-PKcs/Ku70/Ku80 complex assembled on DNA and its implications for DNA DSB repair. *Mol Cell* 22:511–519.
16. Walker JR, Corpina RA, Goldberg J (2001) Structure of the Ku heterodimer bound to DNA and its implications for double-strand break repair. *Nature* 412:607–614.
17. Villarreal SA, Stewart PL (2014) CryoEM and image sorting for flexible protein/DNA complexes. *J Struct Biol* 187:76–83.
18. Boskovic J, et al. (2003) Visualization of DNA-induced conformational changes in the DNA repair kinase DNA-PKcs. *EMBO J* 22:5875–5882.
19. Rivera-Calzada A, Maman JD, Spagnolo L, Pearl LH, Llorca O (2005) Three-dimensional structure and regulation of the DNA-dependent protein kinase catalytic subunit (DNA-PKcs). *Structure* 13:243–255.
20. Yoo S, Dynan WS (1999) Geometry of a complex formed by double strand break repair proteins at a single DNA end: Recruitment of DNA-PKcs induces inward translocation of Ku protein. *Nucleic Acids Res* 27:4679–4686.
21. Hammel M, et al. (2010) Ku and DNA-dependent protein kinase dynamic conformations and assembly regulate DNA binding and the initial non-homologous end joining complex. *J Biol Chem* 285:1414–1423.

22. Suloway C, et al. (2005) Automated molecular microscopy: The new Leginon system. *J Struct Biol* 151:41–60.
23. Scheres SH (2012) RELION: Implementation of a Bayesian approach to cryo-EM structure determination. *J Struct Biol* 180:519–530.
24. Mindell JA, Grigorieff N (2003) Accurate determination of local defocus and specimen tilt in electron microscopy. *J Struct Biol* 142:334–347.
25. Zheng SQ, et al. (2017) MotionCor2: Anisotropic correction of beam-induced motion for improved cryo-electron microscopy. *Nat Methods* 14:331–332.
26. Wu J, et al. (2016) Unsupervised single-particle deep classification via statistical manifold learning. *arXiv*:1604.04539.
27. Kucukelbir A, Sigworth FJ, Tagare HD (2014) Quantifying the local resolution of cryo-EM density maps. *Nat Methods* 11:63–65.
28. Goddard TD, Huang CC, Ferrin TE (2007) Visualizing density maps with UCSF Chimera. *J Struct Biol* 157:281–287.
29. Emsley P, Lohkamp B, Scott WG, Cowtan K (2010) Features and development of Coot. *Acta Crystallogr D Biol Crystallogr* 66:486–501.
30. Adams PD, et al. (2002) PHENIX: Building new software for automated crystallographic structure determination. *Acta Crystallogr D Biol Crystallogr* 58:1948–1954.
31. Chen VB, et al. (2010) MolProbity: All-atom structure validation for macromolecular crystallography. *Acta Crystallogr D Biol Crystallogr* 66:12–21.